JOURNAL OF AIRCRAFT
Vol. 46, No. 1, January–February 2009

Numerical Simulations of a Wingtip Vortex in the Near Field

Matthew J. Churchfield* and Gregory A. Blaisdell†
Purdue University, West Lafayette, Indiana 47907

DOI: 10.2514/1.38086

We investigate the accuracy of current state-of-the-art turbulence models and a compressible Reynolds-averaged Navier–Stokes solver in computing the formation of a wingtip vortex in the near field. The Reynolds-averaged Navier–Stokes solvers used in this investigation are the NPARC WIND 5.0 and Wind-US 1.0 codes. The turbulence models explored are the standard Spalart–Allmaras model, the Spalart–Allmaras model with correction for system rotation and streamline curvature, the Menter shear stress transport model, and the Rumsey–Gatski explicit algebraic stress model. Additionally, we study how solution accuracy is affected by using higher-order numerical schemes as opposed to more grid points. Accuracy is assessed by comparing the results of the wingtip-vortex computations with the data of a reliable, thorough experiment. The solutions obtained using a fifth-order-accurate numerical scheme show that the Spalart–Allmaras turbulence model with corrections for rotation and streamline curvature predicts the mean flow most accurately. However, we find that within the vortex, none of the turbulence models explored accurately captures the magnitudes of the turbulence quantities or the lag of the Reynolds stress components behind the corresponding strain-rate components.

Introduction

WINGTIP vortices, also known as trailing vortices, are formed by any fluid-dynamic surface creating lift. For example, trailing vortices are created by the wings of airplanes, rotors of helicopters, and propellers of ships. In the aviation and aeronautics communities, trailing vortices can pose a significant hazard to aircraft following other aircraft, a common situation during landing and takeoff. Because of the hazard posed, the Federal Aviation Administration and International Civil Aviation Organization (ICAO) require that aircraft following instrument flight rules be separated by a set of minimum distances ranging from 3–6 n mile, depending on the aircraft sizes [1]. With the recent development of the Airbus A380, the ICAO has recommended even greater separation distances for aircraft trailing an A380 during landing and takeoff [2]. In contrast, for aircraft following visual flight rules, separation distance is established at the pilot's discretion because he can see the leading aircraft and thus should be able to judge the location of the leading aircraft's trailing vortices. However, trailing vortices are usually invisible, and all reported trailing-vortex-induced accidents have occurred during visual meteorological conditions. (In fact, trailing-vortex encounters have become a daily event, especially around crowded airports such as those in Europe. For instance, roughly 80 encounters occur at London Heathrow International Airport annually [3].) In the absence of aircraft trailing vortices, it is estimated that a minimum safe separation distance could be as small as 2 n mile [1]. A reduction in separation standards without compromising safety would allow for an increase in the number of takeoff and landing operations from a runway per a given amount of time. This would, in turn, increase airport capacity and reduce congestion. Reviews containing more detailed information about trailing vortices are given by Rossow [1], Gertz et al. [3], and Spalart [4].

To achieve solutions to this problem, wingtip vortices must be better understood. Experimental and computational investigations have been carried out during the past 35 years, yet not all of the important details are well comprehended. For instance, researchers do not completely understand the influence of turbulence on the mean flow and vice versa. Experiments to measure the flow of a wingtip vortex can be costly, difficult, and time-consuming. They are often performed in wind tunnels at Reynolds numbers lower than actual conditions on simplified models rather than on actual aircraft. Measurement difficulties are also created by vortex meander, a phenomenon in which the vortex-core centerline wanders about some location, especially in the far downstream. Currently, though, experiments are the most accurate method of gathering wingtip-vortex data.

On the other hand, computational fluid dynamics (CFD) calculations of wingtip-vortex flows have become capable of yielding high-resolution data for a possibly lower monetary cost than running a wind tunnel. The current CFD method capable of reasonably producing such data at engineering Reynolds numbers is based on the Reynolds-averaged Navier–Stokes (RANS) equations. RANS computations suffer from the fact that a turbulence model is needed to provide closure, and turbulence models historically have had difficulty dealing with highly rotational flow such as that of a wingtip vortex. Other methods such as large eddy simulation (LES) and direct numerical simulation do not have this problem, but they are too computationally expensive at engineering Reynolds numbers to be feasible, especially for computations into the far downstream. A solid understanding of the performance of turbulence models in predicting wingtip-vortex flows is a necessary step toward making the best use of CFD as a tool for studying this important type of flow.

Purpose of This Work

This study examines the performance of various state-of-the-art turbulence models using RANS-based CFD to simulate a wingtip-vortex formation in the near field. The near field is studied because it is thought that if it is not computed accurately, the far field cannot be either. Ultimately, accurate RANS predictions of wingtip-vortex flows are desired deep into the far field in which pinch-off of vortex pairs occurs either naturally or due to some vortex-mitigating design. Furthermore, this study explores the effects of numerical scheme, grid density and topology, and boundary-condition location and type. The computations are compared with experimental data collected in the near field of a wingtip-vortex flow by Chow et al. [5–7]. The knowledge that the current study provides about performing this type of computation lays a good foundation for further work concerning near- and far-field RANS computations of wingtip-vortex flows created by more complex wings. It also provides insight on turbulence modeling of strongly rotating flows.

Received 17 April 2008; revision received 19 June 2008; accepted for publication 20 June 2008.

*Graduate Research Assistant, School of Aeronautics and Astronautics. Student Member AIAA.

†Associate Professor, School of Aeronautics and Astronautics. Senior Member AIAA.

Previous Work

Experiments

Much experimental work has been done both in laboratories and during actual flight to better understand wingtip vortices [1,4]. Only the experiments of Chow et al. [5–7] are discussed here because that flow is computed in this study. This experiment was conducted in the 32 by 48 in. low-speed wind tunnel at the NASA Ames Research Center's Fluid Mechanics Laboratory. Zilliac et al. discuss the turbulence measurements of this experiment in [8]. Chow et al. [5–7] used a half-wing of NACA0012 section with rounded endcaps of a revolved NACA0012 section. The wing's angle of attack was fixed at 10 deg. The chord Reynolds number was 4.6×10^6. Mean measurements were made using a seven-hole pressure probe, and turbulence measurements with a triple-wire anemometer. The half-wing contained over 200 pressure taps for surface pressure measurement. Surface oil-flow visualization was conducted as well. Transition was fixed near the leading edge on both the upper and lower wing and the wingtip using roughness elements. Measurements were made in 12 planes ranging from $1.14c$ upstream of the trailing edge to $0.678c$ downstream of the trailing edge, where c is chord length. This flow is an excellent choice to compute as Chow et al.'s [5–7] experiment was designed with CFD assessment in mind.

Computations

As stated earlier, numerical computation of wingtip-vortex flows are becoming a more useful tool in better understanding wingtip vortices. Dacles-Mariani et al. [9–12] performed one of the more detailed sets of wingtip-vortex computations. Their work was performed in conjunction with the experimental work of Chow et al. [5–7] and Zilliac et al. [8] so that detailed comparisons to the experimentally measured mean and turbulence quantities could be made. Dacles-Mariani et al. [12] identified both numerical error due to discretization and the error associated with the use of eddy viscosity turbulence models. They used an incompressible RANS solver along with the Baldwin–Barth and Spalart–Allmaras one-equation turbulence models. One of their key findings was that at least fifth-order spatial discretization must be used so that the wingtip-vortex-core region is not too diffuse. They also found that the Spalart–Allmaras model gave results similar to those of the Baldwin–Barth model but with more detail. Additionally, use of a rotation correction for their turbulence models greatly improved predictions. For the Spalart–Allmaras model, the production term is originally $\mathcal{P} = C\tilde{\nu}s$, where C is a constant, s is a scalar measure of the deformation rate tensor, and $\tilde{\nu}$ is the working variable for turbulent viscosity; the rotation correction changes the production to $\mathcal{P} = C\tilde{\nu}[|\omega| + 2\ \min(0, |S| - |\omega|)]$, where $|\omega|$ is vorticity magnitude and $|S|$ is strain-rate magnitude. They found that it is important to provide adequately fine grid spacing in the vortex region. A grid with 2.5 million grid points provided the best results, but these results were still not grid independent in the vortex region of the flow. They used the experimental data to set the inflow and outflow boundary conditions. At the outflow boundary, they tried both Dirichlet and Neumann conditions, and they found that Neumann conditions provide more accurate results. In their best case, the core static pressure is overpredicted by 11%, the core velocity magnitude is overpredicted by 3%, and the core size is predicted to within 2%. They attribute the overprediction of core static pressure to the use of one-equation turbulence models that do not model normal Reynolds stresses well. Dacles-Mariani et al. [10] stated that it is "unlikely that anything simpler than a k-ϵ model or full Reynold-stress model has any hope of predicting the flow to within 0.5% accuracy."

Shur et al. [13] performed RANS computations of the following flows: a vortex pair in ground effect with a side wind and a trailing-vortex system behind a civil transport aircraft in high-lift configuration. In the latter computation, wind-tunnel data at some plane behind an aircraft model was used to set the upstream boundary condition, and the flow downstream of that plane was calculated. For these computations, Shur et al. used the standard Spalart–Allmaras turbulence model, the Spalart–Allmaras model with a system rotation and streamline curvature correction proposed in [13–15] and the Menter shear stress transport (SST) model. Their main conclusion is that the rotation and curvature corrected Spalart–Allmaras turbulence model provides much better solutions than the other models tried.

Duraisamy and Baeder [16,17] computed a wingtip-vortex flow with spanwise blowing using a 3.2-million-point grid along with a seventh-order-accurate spatial scheme and the Spalart–Allmaras turbulence model with the rotation correction used by Dacles-Mariani et al. [10]. Although such a high-order numerical scheme was used, their computations predict inaccurate core static pressure and Reynolds stresses. Like others, they attribute the errors to the use of a one-equation turbulence model.

Duraisamy and Iaccarino [18] experimented with applying a frame-rotation and curvature correction to Durbin's [19] v^2-f turbulence model. They used this turbulence model along with a 9.3-million-point grid to compute the wingtip-vortex flow measured by Chow et al. [5–7]. They found that the computations performed with the rotation and curvature corrected v^2-f model are in better agreement with the experiment than those performed with the standard v^2-f model, the Spalart–Allmaras model with Dacles-Mariani et al.'s [10] rotation correction or the Menter k-ω SST model.

Kim and Rhee [20] used the commercial CFD code FLUENT to perform RANS computations of the wingtip-vortex flow of Chow et al. [5–7]. They employed a cell-centered finite volume approach using the QUICK scheme. Two aspects of their investigation are interesting. First, they used an unstructured feature-adaptive grid. This grid automatically adapts to provide higher resolution in the vortex core by identifying regions in which the second-invariant of the rate of deformation tensor falls within a certain range. Second, they used FLUENT's full Reynolds stress transport turbulence model. This was used in addition to the Spalart–Allmaras model with Dacles-Mariani et al.'s [10] rotation correction, the Menter SST model, and the realizable k-ϵ model. With the feature-adaptive mesh and the Reynolds stress transport model, Kim and Rhee [20] obtained good agreement with the experiment forward of the wing's trailing edge, especially in terms of computing low enough vortex-core pressure. However, downstream of the trailing edge, the computed vortex becomes too diffuse. Interestingly, they found that the rotation-corrected Spalart–Allmaras model also provides good results if the correction constants are changed from those which Dacles-Mariani's group used. The Menter SST and the realizable k-ϵ models performed poorly.

LES is becoming an additional tool in the study of wingtip-vortex flows. However, it is still limited to lower Reynolds numbers than seen in most practical applications. Uzun et al. [21] used LES to compute the flow measured by Chow et al. [5–7], but at a Reynolds number an order of magnitude lower than the experiment. They used an overset grid with 24.2 million points. The computations showed marked differences from the experiment, and these differences are attributed to Reynolds number effects. Although LES is a promising method for wingtip-vortex computations, it currently requires far more grid points than RANS to compute flows at much lower Reynolds numbers.

Computational Setup and Flow Physics Modeling

Numerical Solver

The numerical solvers used in this study are two versions of the WIND code [22]: WIND 5.0 [23] and the next iteration of the code, Wind-US 1.0 [24]. The WIND code is created by the NPARC Alliance, a partnership between the NASA John H. Glenn Research Center at Lewis Field and the U.S. Air Force Arnold Engineering Development Center, along with collaboration from The Boeing Company. The first version of WIND became available in 1998, and many validation examples are available.[‡]

WIND numerically solves the full compressible Reynolds-averaged Navier–Stokes equations based on the formulation of Bush

[‡]Data available online at http://www.grc.nasa.gov/WWW/wind/valid/validation.html [retrieved 17 July 2007].

[25]. The governing equations are cast in delta form using a node-centered finite-volume method. The system of discretized mean flow equations are solved by a full block solver. The turbulence equations are solved separate from the mean flow equations. WIND 5.0 only solves the equations on a single- or multiblock structured grid, whereas Wind-US 1.0 is capable of solving on unstructured grids, as well. In this study, only structured grids are used. Steady-state solutions are obtained using Euler implicit local time stepping at a constant Courant–Freidrichs–Lewy (CFL) number. In most cases, a CFL number of 1.3 is used; however, if the solution becomes unstable, CFL values as low as 0.5 are used to regain stability.

In the discussion to follow, the spatial numerical scheme refers to the way WIND computes the convective and pressure components of the flux seen in the integral form of the mean flow equations. In this study, we specify that WIND use the upwind-biased Roe's flux-difference-splitting scheme [26] with second- up to fifth-order spatial discretization accuracies. The second-order-accurate version of this scheme, though, only holds its formal order of accuracy on stretched Cartesian grids, and the higher-order versions only hold theirs on unstretched Cartesian grids. The viscous flux term is solved using second-order central differencing for all cases, and the convective fluxes of the turbulence model equations are discretized with a first-order upwind method. The mean flow solution at wall boundaries is second-order-accurate regardless of the scheme specified. Therefore, if the scheme specified is fifth-order-accurate, for example, the solution is not truly of this order of accuracy. However, clear benefits of using the higher-order schemes have been observed.

In this study, each case is computed in parallel with five iterations per cycle. However, one iteration per cycle is used if the spatial discretization is fifth-order to maintain stability. After every cycle, information is shared amongst the abutting or overlapping computational zones. Computations are performed on up to three dual-processor dual-core nodes (4 processors/node) of a Linux cluster.

Convergence is monitored by observing both the l^2 norm of the governing equation residuals and values of the integrated pressure and viscous forces on various small areas (four abutting grid cell faces) on the half-wing surface versus iteration count. When the residuals oscillate about some constant and the forces become steady, convergence is achieved. It is found that using a CFL number of 1.3, fifth-order spatial discretization, a 5.3×10^6 point grid divided into 11 zones, and a flowfield initialized to freestream conditions, roughly 100,000–120,000 iterations are necessary for convergence, which requires about three weeks of computation time on the aforementioned processors. Many iterations are necessary to propagate the wingtip-vortex downstream, allow it to interact with the outflow boundary, and then to let those interactions propagate back upstream to the wing.

Computational Geometry

Because we compute the wingtip-vortex flow measured by Chow et al. [5–7], the computational domain must mimic that of the experiment as closely as possible. The overall geometry used in this study, as shown in Fig. 1, is a rectangular prism that represents the flowfield occupying the interior volume of the wind-tunnel test section. This geometry includes a nonswept, nontapered, nontwisted half-wing attached at its root to a vertical wall of the tunnel. The half-wing is of symmetric NACA 0012 section and the wingtip is a half body of revolution of the same section. It has a chord of 48 in. and measures 36 in. from root to the wingtip apex. The wind-tunnel section is 48 in. wide by 32 in. tall. The half-wing is attached at its quarter-chord midway up one of the vertical walls, and it is pitched up 10 deg. The domain extends $2.5c$ forward and $3.0c$ aft of the half-wing's trailing edge, but these dimensions do not reflect the actual test section length. The streamwise extent of the computational domain is greater than that of Chow et al's [5–7] measurements (extended from $1.135c$ upstream to $0.678c$ downstream of the trailing edge) to assure that the computed solution is free of boundary effects where comparison with the experiment can be made. A Cartesian coordinate system is used, and the origin lies at the trailing-edge root of the half-wing. The orientation of the coordinate system is shown in Fig. 1.

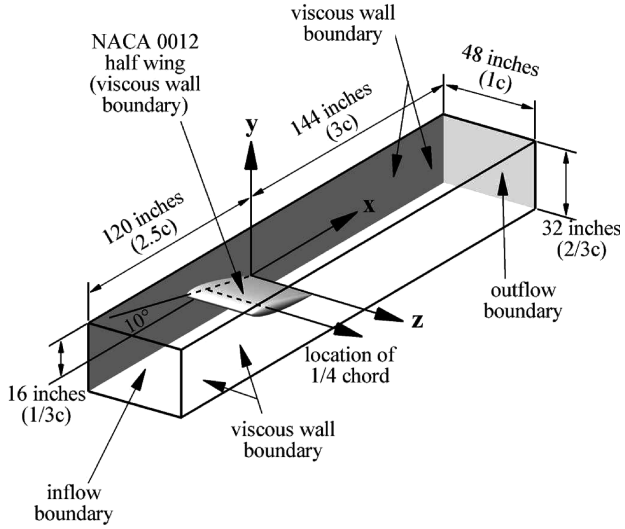

Fig. 1 Overall view of the domain geometry used in the computation.

Boundary Conditions

The inflow boundary conditions are set using WIND's freestream boundary-conditions option. To enforce the freestream boundary conditions, WIND "uses one-dimensional characteristic theory to set boundary flowfield variables from freestream conditions, based on the flow direction at the boundary" [23]. There is an option to either hold constant the total pressure, total temperature, and local flow angles or the total pressure and characteristic values. In the process of applying the conditions, WIND may adjust the Mach number over the boundary. The values specified in this study are that Mach number, static pressure, and temperature are set to 0.14027, 15.9098 psi, and 521.0522°R initially, and the characteristic values are held constant. This causes the computational reference conditions to be the same as Chow et al.'s [5–7] when convergence is achieved, and those conditions are axial velocity $U_{\text{ref}} = 170.0$ ft/s and chord Reynolds number $Re_c = 4.6 \times 10^6$. The reference location, to the best of the authors' knowledge, is at $x = -1.1344c$, $y = 0.3423c$, and $z = 1.0492b$, the only location in Chow et al.'s data set where $U/U_{\text{ref}} = 1.0$. b is the half-span of the wing, and U, V, and W are the x, y, and z components of mean velocity, respectively. Because the reference conditions in the experiment were not taken at the same location as the inflow boundary, the inflow boundary conditions and the corresponding outflow mass flow rate must be manually iterated until the conditions at the reference location match those of the experiment.

Over the outflow boundary, the mass flow rate is set to equal that of the specified inflow boundary with a value of 136.42 lbm/s. WIND extrapolates quantities to the outflow boundary using zeroth- or first-order extrapolation. (Zeroth-order extrapolation is used in this study because when using WIND 5.0, first-order extrapolation causes the vortex-core pressure to sharply increase just upstream of the outflow boundary, no matter where the boundary is located. Furthermore, using Wind-US 1.0, first-order extrapolation causes the solution to diverge. The solutions computed using WIND 5.0 and Wind-US 1.0 agree when using zeroth-order extrapolation and all other conditions are the same.) Then the boundary mass flow rate is found with numerical integration and a correction factor is computed. The outflow boundary momentum is updated using the correction factor. Finally, energy at the boundary is updated to be consistent with the updated momentum and extrapolated quantities. This mass-flow-rate boundary condition allows pressure to vary over the boundary surface [23,24], which is important because the vortex exits the domain on this boundary and its core exhibits a lower pressure than

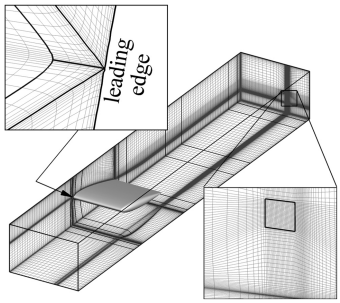

Fig. 2 Overall view of the computational grid.

the surrounding flow, and so pressure variation over the boundary is important.

The remaining exterior boundaries lie on the wind-tunnel walls and the wing surface, and they are specified to be viscous walls in which the no-slip and zero-normal pressure-gradient conditions are met. WIND does not use a correction to the zero-normal pressure-gradient condition if the wall is curved.

In all cases, the domain is divided into 11 zones with overlapping internal zone boundaries to enable parallel processing. The grids overlap by eight points so that each zone involved in the overlap has four fringe-point planes. Fringe points receive their information from the interior of the adjacent zone. Each fringe point from one zone matches up exactly to a corresponding interior point of another zone so that no interpolation is necessary during zonal information sharing.

Computational Grid

After experimenting with different grid topologies previously [27,28], we decided to use grids of H-topology, which are well suited to the rectangular shape of this computational domain. Two H-grids were created: the coarse grid has half as many points as the fine grid. Because the fine grid is used for the final computations, only the details of that grid are discussed. The fine grid is shown in Fig. 2. It contains 5.3×10^6 points; 290 of the grid planes are in the x direction, 151 are in the y direction, and 121 are in the z direction. There are 84 streamwise grid planes downstream of the wing's trailing edge and 101 over the wing.

The wing's boundary-layer grid resolution is listed in Table 1. The grid exhibits $y_2^+ \leq 1$ over the wing surface, where y_2^+ is the $y^+ = d\sqrt{\tau_w/\rho_w}/\nu_w$ value at the first grid point away from the wall. Here, d is the distance normal from the wall, τ_w is the shear stress, ρ_w is the density, ν_w is the kinematic viscosity, and the subscript w refers to values at the wall. The highest y_2^+ values over the wing surface are seen at the upper outboard trailing edge underneath the wingtip vortex, which causes the boundary layer to be thin in that region. The grid contains roughly 12 grid points in wall-normal grid lines within the boundary layer at the wing's leading edge. This low number of normal grid points only exists at the leading edge, after which the number quite rapidly increases until roughly the quarter-chord. After the quarter-chord, a more gradual increase is seen. The upper trailing edge contains 50 points along one wall-normal grid line within the boundary layer, and the lower trailing edge contains 22. However, the region under the wingtip vortex at the upper outboard trailing edge only contains 20 points along a wall-normal grid line in the boundary layer, due to the boundary layer's thinness there. The upper left inset of Fig. 2 shows how the grid is constructed very near the wing surface at the leading edge of the wing and wingtip.

Boundary layers also exist on the wind-tunnel walls. The normal grid spacing at the wall in these boundary layers is $5.0 \times 10^{-6}c$, such that the y_2^+ values are approximately one in most places. They contain roughly 10 grid points in the wall boundary layers at the entrance and between 20 and 30 at the exit. Streamwise spacing is relatively large because the streamwise gradients are small.

Correctly resolving the wake sheet behind the half-wing is important because the wake is rolled into the vortex. The streamwise-running grid lines in the upper and lower wings' boundary layers become the grid lines of the wake beyond the trailing edge. Because the wake expands with downstream distance, the cross-stream grid spacing in the wake sheet linearly expands along its centerline from $5.0 \times 10^{-6}c$ at the wing's trailing edge to $5.0 \times 10^{-4}c$ at $x = 2.5c$; the wake cross-stream spacing then remains constant.

The best method found for estimating the vortex-core location is to simply use the experimental location measured by Chow [6] and to create the computational grid accordingly. If experimental data were not available, one could iteratively refine the grid or use an adaptive grid. The spacing and number of grid points in the vortex core used by Dacles-Mariani et al. [11] is used as a guideline in this study. The vortex-core grid spacing used here is given in Table 2. The estimated core radius r_c is $2.083 \times 10^{-2}c$, and so a rectangular prism of grid points of square cross section that circumscribes the radius is used to encompass the estimated core region. The core radius is defined as the radial distance from the vortex centerline to the location of maximum crossflow velocity: $U_{yz} = \sqrt{V^2 + W^2}$. The information in Table 2 refers to the grid points within this rectangular volume encompassing the estimated core. The lower right inset of Fig. 2 shows a cross-stream plane of grid points from the grid near the estimated vortex core. Notice the square region that is meant to encompass the vortex core and that grid lines from the estimated wake region are expanded to bring more grid lines into the core region.

Finally, the streamwise spacing of the grid is reduced as the grid lines approach the outflow boundary to minimize the effect of the outflow boundary on the flow upstream of it.

Turbulence Models

Four of the turbulence models that are supplied with WIND are explored: the Spalart–Allmaras model in both standard form (SA) [29,30] and with the Spalart–Shur correction for system rotation and streamline curvature (SA-RC) [13–15], the Menter SST k-ω model [31,32], and the Rumsey–Gatski k-ϵ algebraic Reynolds stress model (ASM) [33–35]. The ASM is only coded into Wind-US 1.0, whereas all of the other models are coded into both versions of WIND.

The one-equation SA model consists of a transport equation for turbulent viscosity. The Reynolds stress tensor is derived from the Boussinesq approximation:

$$R_{ij} = \tfrac{2}{3}k\delta_{ij} - 2\nu_t(S_{ij} - \tfrac{1}{3}S_{kk}\delta_{ij}) \tag{1}$$

where R_{ij} is the Reynolds stress tensor, k is the turbulent kinetic energy, δ_{ij} is the Kronecker delta, ν_t is turbulent kinematic viscosity, $S_{ij} = 0.5(\partial U_i/\partial x_j + \partial U_j/\partial x_i)$ is the strain-rate tensor, and U_i and x_i are the ith components of the mean velocity and coordinate system vectors. Because k is not computed by the SA model, the $(2/3)k$ term used in computing normal Reynolds stresses is ignored [29].

The SA-RC model is the standard SA model with a rotation function f_{r1} multiplying the production term of the equation for the turbulent viscosity working variable $\tilde{\nu}$. This rotation correction is

Table 1 Grid spacing in the wing boundary layer

Leading-edge spacing	
Normal	$1.0 \times 10^{-6}c$
Streamwise	$1.0 \times 10^{-6}c$
Trailing-edge spacing	
Normal	$5.0 \times 10^{-6}c$
Normal (tip region)	$2.0 \times 10^{-6}c$
Streamwise	$1.0 \times 10^{-4}c$

Table 2 Grid spacing in the vortex core

Cross stream	$2.083 \times 10^{-3}c$
Streamwise at the trailing edge	$1.0 \times 10^{-4}c$
At $x = 0.667c$	$5.2 \times 10^{-2}c$
At $x = 3.0c$	$1.46 \times 10^{-4}c$
Points across the estimated core	21

empirical, Galilean-invariant, and relies upon tracking the direction of the principal axes of the strain-rate tensor. The details of this rotation correction are found in [13–15].

The two-equation SST model is formulated like the Wilcox k-ω model in the inner region of the boundary layers and like the standard k-ϵ model outside of that region. The ϵ equation of the k-ϵ model is cast as an ω equation, resulting in an extra term, called the cross-diffusion term: $\rho\sigma_\omega\omega^{-1}(\partial k/\partial x_j)(\partial\omega/\partial x_j)$. In this term, σ_ω is a model constant and ω is the specific dissipation rate. A blending function is used to deactivate the cross-diffusion term within the inner region of the boundary layer. Also, the model attempts to account for the transport of the principle Reynolds shear stress by limiting its rate of change. Turbulent viscosity is calculated from k and ω, and the Reynolds stress tensor is computed using the Boussinesq approximation of Eq. (1).

The ASM model, as coded in Wind-US 1.0, is based on a k-ϵ model. Turbulent viscosity is calculated from k and ϵ, but a nonlinear algebraic relationship is used to compute the Reynolds stress tensor instead of the Boussinesq approximation. This nonlinear relationship is different from those used in nonlinear turbulent viscosity models because it is a direct simplification of a full Reynolds stress model. Therefore, it contains some of the turbulence physics that full Reynolds stress models have but that turbulent viscosity models such as the SA and SST models lack. The hope is that it will naturally capture some of the effects of rotation on the turbulence of the vortex.

To induce transition to turbulence, Chow [6] affixed a $\frac{1}{8}$-in.-wide line of 0.017-in.-diam roughness elements to the wing across the upper and lower spans at an arc distance of 2.0 in. from the leading edge. WIND controls transition by adding an increasing percentage of the computed turbulent viscosity to the molecular viscosity at each successive streamwise grid point in a user-specified transition region along a viscous wall. In this study, transition is specified to occur across one grid cell at the same location as Chow's roughness elements, and this is verified by observing an abrupt increase in contours of skin-friction coefficient over the wing surface.

Results

Spatial and Numerical-Scheme Convergence

As others [11,16–18] have found, the computed wingtip vortex is very sensitive to grid refinement and spatial numerical-scheme order of accuracy. In our previous work [27,28], grid independence was not attained by using the fine grid along with a spatially-second-order-accurate numerical scheme. Rather than creating an even finer grid, using spatially-higher-order-accurate upwind-biased numerical schemes and the fine grid seemed to be the most efficient approach. Although not the same as computing upon a finer mesh, using WIND's higher-order versus second-order-accurate upwind-biased Roe's flux-difference-splitting scheme provides a more resolved solution and requires little extra computation time. By comparison, doubling the number of grid points to make a finer grid may more than double the computation time. Pressure along the vortex-core centerline and on the wing surface beneath the forming vortex are sensitive quantities and are useful to observe when assessing the effect of changing the grid density or spatial order of accuracy. The vortex-core centerline is located using Tecplot 11's vortex-core finder, which uses the method of Haimes and Kenwright [36].

Figure 3 shows the effect on core centerline pressure caused by changing the spatial order of accuracy of the numerical scheme from second through fifth when the fine grid and the SA-RC turbulence model are used. This plot shows that the solution becomes less accurate when changing the scheme from second to third order. Only the second-order version of the scheme is modified to hold its formal accuracy on stretched grids, which may explain the drop in accuracy when changing to the third-order scheme with no modification for stretched grids. A great improvement occurs when changing from third- to fourth-order accuracy. Little change happens when changing from fourth- to fifth-order accuracy, especially in the region in which experimental data were taken.

The effect of changing spatial order of accuracy on wing-surface pressure is shown in Fig. 4. The surface just inboard of the wingtip

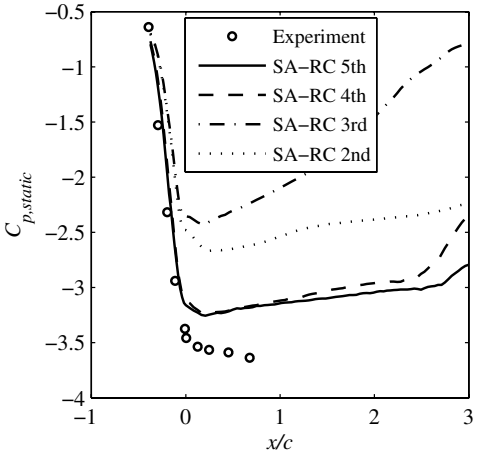

Fig. 3 Effect of increasing the spatial order of accuracy on $C_{p,\text{static}}$ in the vortex core using the fine grid and the SA-RC turbulence model.

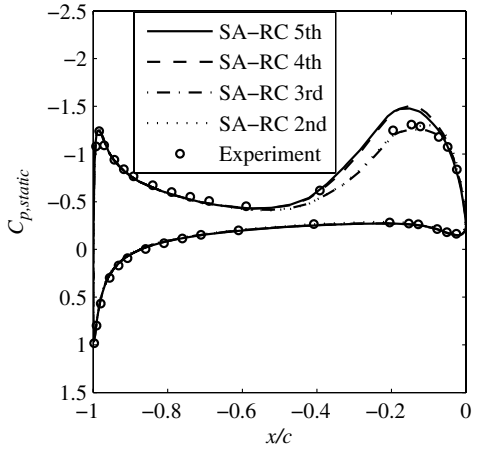

Fig. 4 Effect of increasing the spatial order of accuracy on the wing surface $C_{p,\text{static}}$ at a spanwise location of $z = 0.889b$ using the fine grid and the SA-RC turbulence model.

seems to be the location most sensitive to changes in spatial order of accuracy, and so the surface pressure in a plane located at $z = 0.889b$ is shown. The plot shows that the difference between the fourth- and fifth-order-accurate solutions is small; however, the fifth-order-accurate solution agrees less well with the experiment than does the second-order-accurate case. This inaccuracy is not due to the spatial scheme (because the solution is nearly unchanged as the scheme is changed from fourth to fifth order), but rather may come from turbulence modeling.

Changing the grid density while using the spatially-fifth-order-accurate numerical scheme and the SA-RC model also affects the pressure along the vortex-core centerline. Figure 5 shows the coefficient of static pressure along the core using the coarse and fine grids. Included is an estimate of the solution with the leading-order error eliminated using Richardson extrapolation [37]. The leading error term is assumed to be of order Δh^5, where Δh is the grid spacing, and the grid-spacing ratio between the grids is $\sqrt[3]{2}$. The region near the downstream boundary ($x > 2.25c$) should be disregarded at this point because it is influenced by the outflow boundary condition, and it is beyond the region in which comparison with experimental data can be made. Disregarding that boundary region, the results lie farther from the experimental data as the grid is refined. It is coincidental that the results obtained with the coarse grid are in better agreement with the experimental data than those obtained with the fine grid. A 3.9% maximum change in magnitude of $C_{p,\text{static}}$ is observed at $x = 0.2c$ between the coarse- and fine-grid solutions. Richardson extrapolation estimates a further change of 1.8%. As another example, at the same location, the magnitude of

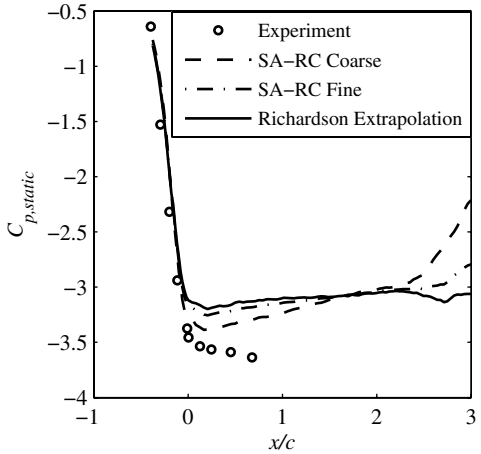

Fig. 5 Effect of increasing the grid point density on the $C_{p,\text{static}}$ in the vortex core using the SA-RC turbulence model and a spatially-fifth-order-accurate numerical scheme.

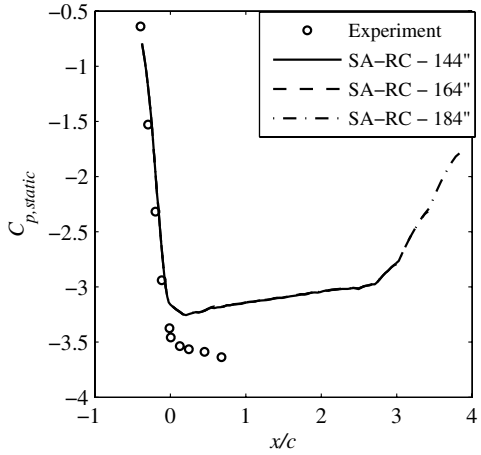

Fig. 6 Effect of increasing the outflow boundary distance from the trailing edge on $C_{p,\text{static}}$ in the vortex core using the SA-RC turbulence model and a spatially-fifth-order-accurate numerical scheme.

axial velocity changes by 2.8% between the coarse and fine grid. Richardson extrapolation causes a further 1.3% change in magnitude, which is a small change. Because this grid refinement process along with Richardson extrapolation shows the solution to be nearly grid-independent along the vortex-core centerline, the solution error in this region is most likely due to turbulence modeling.

Based on the changes to the solution by removing leading-order error as estimated with Richardson extrapolation, the fine grid and the spatially-fifth-order-accurate numerical scheme seem to provide enough grid and numerical scheme independence that the effects of different turbulence models can be well assessed. From this point forward, all cases considered use the fine grid and the spatially-fifth-order scheme.

Boundary and Zone Coupling Effects

In this study and during our previous work [27,28], the effect of different types of outflow boundaries has been studied. One of the boundary conditions tried is to specify a uniform static pressure over the entire outflow boundary. This type proves unrealistic because the low pressure in the vortex core cannot be captured at the boundary. Also, a condition was tried with some success in which pressure at one boundary point is specified, and the pressure at the rest of the boundary points depends on that specified pressure and the flow upstream. The difficulty with this condition, though, is that the correct pressure must be specified at that one point, which requires manual iteration. The method that works best is to specify the mass flow rate at the outflow boundary to be the same as that of the inflow boundary. This type of boundary condition allows pressure on the outflow boundary to vary naturally without requiring the user to specify the pressure at one point, and so it is best suited to this flow.

The location of the outflow boundary also can affect the solution. The location of that boundary was set at $x = 3.00$, 3.42, and $3.83c$, and the effects on the vortex-core centerline pressure are shown in Fig. 6. Pressure for all three cases coincide nearly exactly, except very near their corresponding outflow boundaries. In the region in which comparison with experimental data can be made, almost no difference in the three solutions is observed. The same behavior occurs for other flow quantities, including axial velocity and vorticity, total pressure, and core radius and position. Therefore, extending the boundary to only $3.00c$ past the wing's trailing edge is adequate and uses the least number of grid points. The boundary could probably be moved closer to the farthest downstream experimental measurement plane without changing the solution, but observation of the behavior of the computed vortex a moderate distance beyond that plane is desired.

In Fig. 6, an abrupt increase in vortex-core static pressure beyond $2.75c$ can be observed; it occurs because the vortex core begins to exit the highly refined region of the grid meant for the vortex. The lower grid resolution causes the vortex to diffuse unphysically resulting in the pressure increase. We did not adjust the grid to follow the vortex core in this region because it is far downstream of where Chow [6] took experimental data, and so no useful comparison with the experiment can be made.

In this study, overlapping internal boundaries are used rather than abutting ones, because the previous experience [27,28] of the authors shows that although abutting zones work well if the numerical scheme is of second-order accuracy, the solution exhibits discontinuities across the abutting boundaries if higher-order schemes are used. With the quadruple fringe overlap used in this study, the solution smoothly varies across internal zone boundaries.

Mean Flow Results

From this point forward, the four turbulence models are compared. All computations are with the spatially-fifth-order-accurate Roe's flux-difference-splitting scheme. Each computational case is referred to by the abbreviation for the turbulence model used: SA, SA-RC, SST, or ASM. The mean flow results are best examined in three separate regions: on the wing surface, above the wingtip on which the primary vortex and the much weaker secondary and tertiary vortices form, and downstream of the wing in which the fully formed wingtip vortex develops and becomes fairly axisymmetric.

Wing Surface

The mean solution over the wing surface is important because the boundary layer that forms there provides the vorticity necessary for the wingtip vortex to form and grow. Profiles of the coefficient of static pressure $C_{p,\text{static}}$ at two spanwise locations on the wing surface are plotted in Fig. 7. That quantity is defined as $C_{p,\text{static}} = (p_{\text{static}} - p_{\text{static,ref}})/q_{\text{ref}}$, where $q_{\text{ref}} = 0.5\rho_{\text{ref}}U_{\text{ref}}^2$, and the subscript ref refers to conditions at the experimental reference location at $x = -1.1344c$, $y = 0.3423c$, and $z = 1.0492b$. The experimental pressure distribution is similar to that of an infinite span wing for the inboard portion of the half-wing. Toward the tip, however, there is a band of low pressure on the aft top of the wing, which exists due to the formation of the wingtip vortex above that location. In Fig. 7, the profile at $z = 0.167b$, which is near the wing root, shows that all the computational results are very accurate and consistent. In contrast, the results at $z = 0.889b$ show that the four cases are inconsistent. All of the models incorrectly predict the low-pressure band. They all predict too low a pressure, but the results from the SA-RC case are in best overall agreement. The SST and SA cases exhibit a low-pressure band that is too short in the axial direction, hinting at the diffuse vortex they predict, whereas the SA-RC and ASM cases exhibit a band nearly the same length as in the experiment.

The direction that viscous stresses act on the wing surface can be visualized by surface streamlines created by an oil-flow experiment.

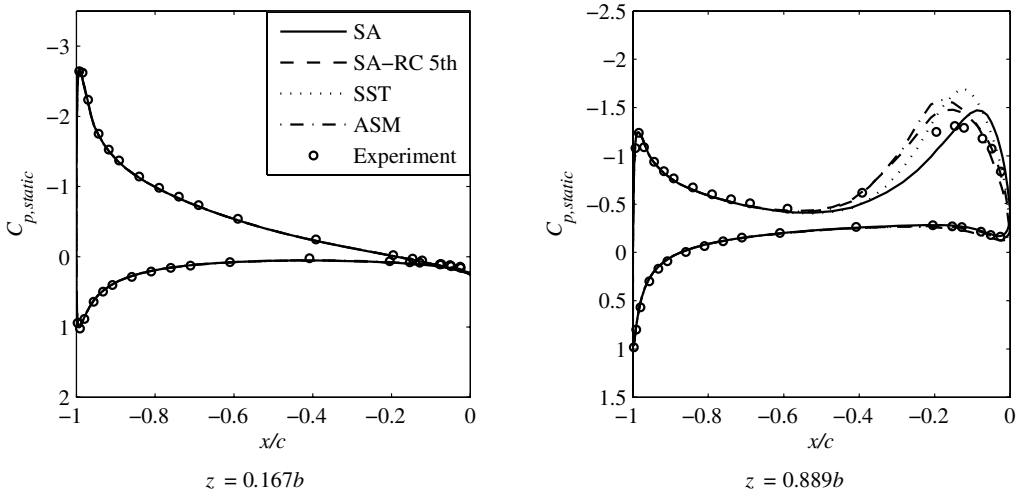

Fig. 7 Profiles of $C_{p,\text{static}}$ over the wing surface at two spanwise locations.

Chow [6] performed an oil-flow visualization on the surface of his wing and identified primary and secondary separation and attachment lines, as shown in Fig. 8. The primary separation line runs in the flow direction along the rear half of the wingtip, and the primary attachment line is inboard and parallel to the separation line. The primary separation line denotes separation of the flow migrating from the pressure to the suction side of the wing as it passes over the wingtip. This separated flow reattaches at the primary attachment line. The rotational flow associated with this separating boundary layer is the start of the wingtip vortex measured by Chow. Between the primary lines are secondary separation and attachment lines, which suggest the existence of secondary and tertiary vortices: the secondary vortex rotating counter to the primary vortex and just outboard of it and the tertiary vortex rotating in the same sense as the primary vortex and even farther outboard.

Figure 8 also shows simulated oil-flow visualizations of the computational data on the wing's upper surface. This visualization technique uses a version of the line-integral-convolution (LIC) method of Cabral and Leedom [38], which is modified by Tricoche et al. [39], to create oil-flow-like streaks on the wing's surface. Then, using Tecplot, that LIC image is overlaid with opaque contours of shear stress magnitude on the wing's surface, for which darker colors denote higher stress. This process simulates the enhanced scouring of light-colored oil in areas of higher stress, leaving darker areas. In each case, there is a region just inboard of the aft tip of the wing on which the surface streamlines are swept outward toward the tip and the surface appears darker. Those streamlines lie directly below the primary vortex. Here, the primary vortex creates high crossflow velocity near the wing surface along with a thin boundary layer, both of which increase the velocity gradient and hence the shear stress at the surface. These shear stresses sweep the streamlines toward the tip, as Fig. 8 shows. All computational cases show the primary and secondary separation and attachment lines. In the experiment, the secondary lines are very close together; the only case that captures that is the SA case. However, the SA and SST cases exhibit too large a distance between the secondary separation line and the primary attachment line. Also, the dark high-stress region of the SA and SST cases is too axially short. In these respects, the SA-RC and ASM cases match the experiment most closely.

Vortex Formation

As discussed previously, when the flow migrates from the pressure side to the suction side of the wing, it separates at the wingtip. Here, the primary vortex forms along with the weaker secondary and tertiary vortices. This occurs roughly between $-0.5c < x < 0$ in the experiment. In this section, the stage of formation in a plane at $x = -0.113c$ is examined because it is a good example of what happens in the other parts of the formation region. Contours of crossflow velocity magnitude $U_{yz} = \sqrt{V^2 + W^2}$ are used for comparing the computations with the experiment, as shown in Fig. 9. To identify the primary vortex, streamlines in this plane are also plotted; however, the secondary and tertiary vortices are not clearly identified. The choice of cutting-plane orientation greatly influences which flow details are identified with streamlines within that plane. Unfortunately, the experimental data are given only in planes of constant x, an orientation that does not clearly show the secondary and tertiary vortices. These, however, are the only planes in which computed streamline details can be compared with the experiment. Later in this section, though, the computed secondary and tertiary vortices will be shown more clearly, but in a way in which comparison with the experiment is not possible. A clear, concise

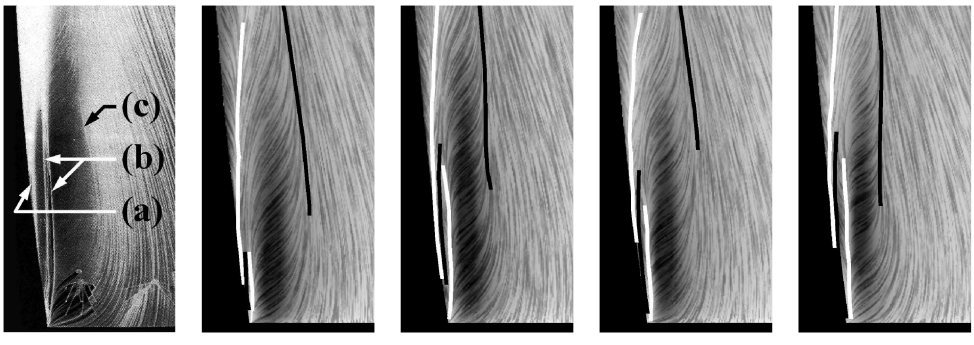

Fig. 8 Surface streamlines on the upper aft surface of the wingtip and contours of surface shear stress magnitude; separation lines (white) and attachment lines (black) for the primary separation line (a), secondary attachment and separation lines (b), and primary attachment line (c) (photo is reproduced from Chow's [6] experiment with the author's permission).

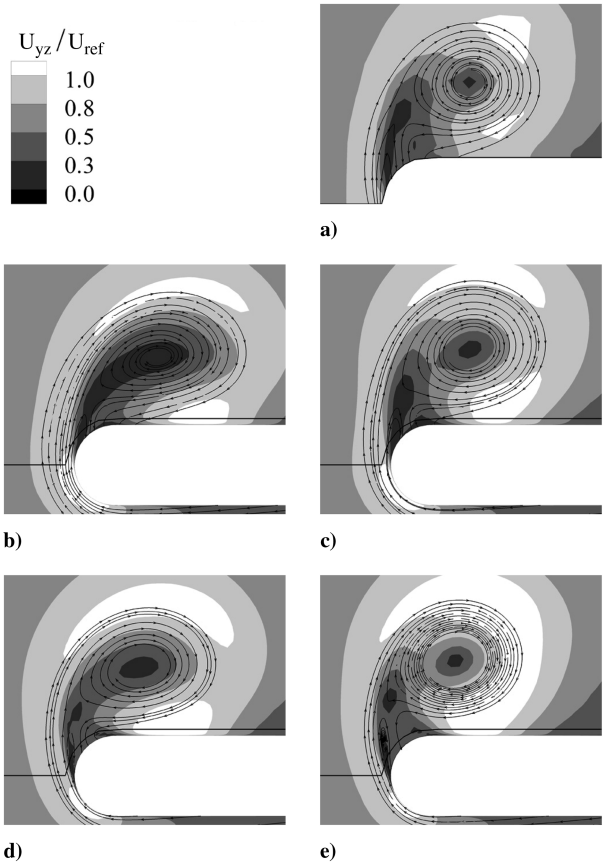

Fig. 9 Contours of crossflow velocity normalized by reference velocity and streamlines in the y–z planes: a) experiment, b) SA, c) SA-RC, d) SST, and e) ASM; contours are viewed from downstream looking upstream.

discussion of exploration of three-dimensional vortex data sets using cutting planes, and their proper orientation, is given by Tricoche et al. [40].

The SA and SST models, which both rely on the Boussinesq approximation and do not have a rotation correction, predict the primary vortex to have streamlines that are elliptical in shape, which does not compare well with the round shape of the experimental primary-vortex streamlines. In contrast, both the SA-RC and ASM cases exhibit fairly round streamlines. Unlike the experiment, the SA case does not exhibit two distinct low-U_{yz} regions, one in the primary-vortex core and the other where the flow separates along the primary separation line; rather, these regions blend together. The U_{yz} contours of the SA-RC case match the experimental contours well, whereas the contours in the ASM case are similar in shape to those of the experiment but exhibit peaks of U_{yz} that are too large in magnitude.

The secondary separation and attachment lines seen on the wing surface suggest the existence of secondary and tertiary vortices in the flow. The second invariant of the velocity gradient tensor, $\mathrm{II} = 0.5(\Omega_{ij}\Omega_{ij} - S_{ij}S_{ij})$, where S_{ij} and Ω_{ij} are the strain-rate and rotation-rate tensors, respectively, is a good indicator of vortices in the flow. In rotation-dominated regions, such as a vortex, $\mathrm{II} > 0$. Because the SA-RC model performs best, data from that case are used in this discussion. Superimposing streamwise contour slices of II on a picture of the wing surface with surface streamlines (fine white lines) shows secondary and tertiary vortices in addition to the primary vortex, as shown in Fig. 10a. The primary vortex is identifiable because it is the largest in radius and has the greatest values of II. The secondary vortex lies between the secondary separation and attachment lines, and the tertiary vortex lies just inboard of the primary separation line. Separation and attachment lines are shown as heavy white and black lines, respectively.

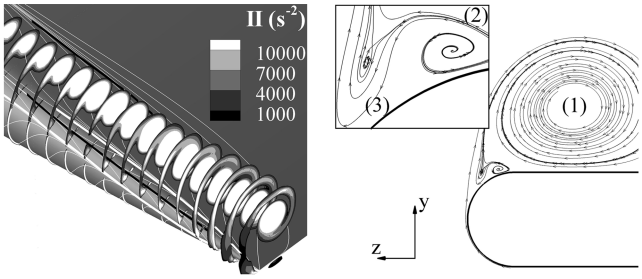

Fig. 10 Secondary and tertiary vortices from the SA-RC case: a) contour slices of II, wing surface streamlines, and separation/attachment lines and b) streamlines in a cutting surface normal to the wing at $x = -0.146c$ viewed from downstream looking upstream.

Another way to visualize the secondary and tertiary vortices is to look at streamlines constrained to cutting planes in the flow. As Tricoche et al. [40] discussed, the orientation of these cutting planes is important in identifying various flow features, such as vortices. Earlier, we mentioned the fact that plotting streamlines in constant x cutting planes only identifies the primary vortex. Therefore, a better orientation is to have the cutting surface extend perpendicularly to the wing surface and aligned with the z direction. A cutting plane oriented in this way along the chord of the wing at $x = -0.146c$ clearly shows the secondary and tertiary vortices, in addition to the primary vortex, as shown in Fig. 10b. The primary vortex is largest and is labeled (1), whereas the secondary and tertiary vortices, labeled (2) and (3), are smaller in radius and have more elliptical secondary streamlines. The secondary vortex rotates counter to the primary vortex; the tertiary vortex rotates in the same sense as the primary vortex. The secondary streamlines indicate that the tertiary vortex extends over a shorter axial region than the secondary vortex.

Downstream Development Along the Vortex Centerline

One way to observe the downstream development of the vortex is to plot various mean quantities along the vortex centerline, as shown in Fig. 11. Those quantities are plotted from about $0.4c$ upstream to $3c$ downstream of the trailing edge. In this region, the secondary and tertiary vortices merge with the primary vortex, and the primary vortex becomes nearly axisymmetric with downstream distance. As in the vortex-formation region, the differences among computational cases are clear, with the SA-RC and ASM cases performing best.

Static Pressure. Figure 11a shows the coefficient of static pressure along the vortex core. Upstream of $x = -0.1c$ the results from each case are similar. Beyond that location, the pressures computed by the various cases diverge from one another. The SA-RC and ASM cases continue to exhibit a decrease. However, $C_{p,\mathrm{static}}$ in the SST case quickly increases, and beyond $x = 0.5c$ it asymptotically approaches $C_{p,\mathrm{static}} = 0$. Static pressure in the SA case increases similarly, but at a slightly slower rate with increasing x. The centerline $C_{p,\mathrm{static}}$ predicted in the ASM case decreases to a minimum of -3.8 at the trailing edge, which is even lower than the experiment. It then begins to increase similarly to that of the SA and SST cases. The SA-RC case predicts a pressure decrease to a minimum of $C_{p,\mathrm{static}} = -3.3$, which is 9.4% higher than the experimental value. After the minimum, $C_{p,\mathrm{static}}$ in the SA-RC case is nearly constant from $0.2c < x < 2.7c$, only rising by 0.3 units. Although the experimental core pressure appears to level off around a lower value of $C_{p,\mathrm{static}} = -3.6$, the SA-RC model's behavior is similar to that of the experiment in the region in which comparison can be made. The SA-RC centerline $C_{p,\mathrm{static}}$ data are very similar to Dacles-Mariani et al.'s [11] computed results. They used an SA-RC turbulence model with a simpler rotation correction than that used in this study. Dacles-Mariani et al. explained that the computed core $C_{p,\mathrm{static}}$ is higher than that of the experiment, possibly because one-equation turbulence models, such as the SA and SA-RC models,

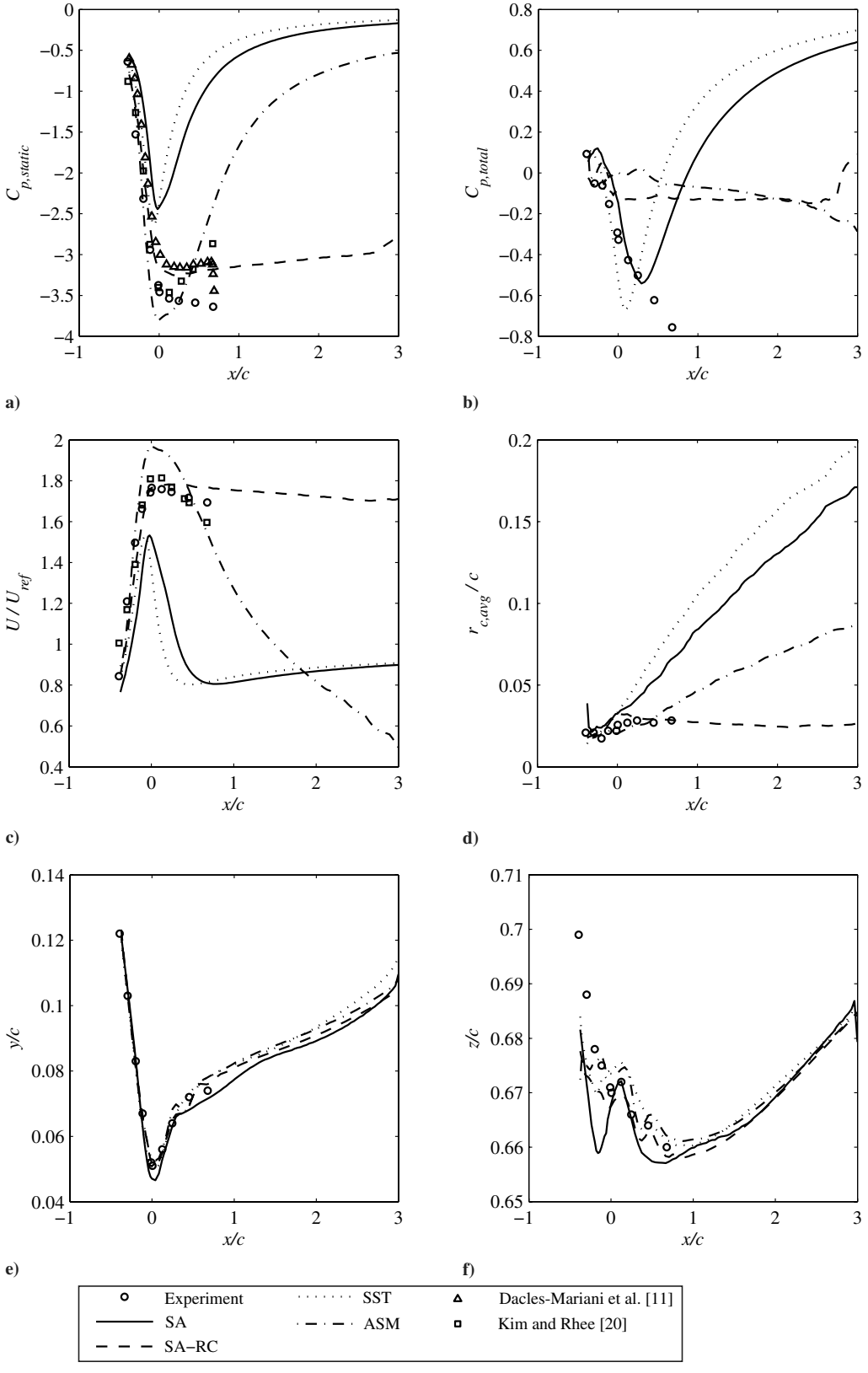

Fig. 11 Various mean quantities along the vortex-core centerline: a) $C_{p,\text{static}}$, b) $C_{p,\text{total}}$, c) U/U_{ref}, d) $r_{c,\text{avg}}/c$, e) x–y location, and f) x–z location.

neglect the $(2/3)k$ term in the Boussinesq approximation [Eq. (1)]. This causes the normal Reynolds stresses to be smaller than they should be or negative, which in turn affects the momentum equations by raising the pressure by $(2/3)k$. The ASM model, which is a two-equation model that uses a nonlinear relation to compute R_{ij}, does include the $(2/3)k$ term, and it exhibits lower minimum pressure than the SA-RC model, reinforcing the explanation of Dacles-Mariani et al. However, the SST model is also a two-equation model, and it does not exhibit lower minimum core static pressure than the SA-RC model. Also, note that Dacles-Mariani et al.'s centerline $C_{p,\text{static}}$ drops rapidly at the downstream end of their domain. This is because they imposed the experimental data as their outflow boundary condition, which is different from the mass flow boundary condition used in this study.

Total Pressure. The coefficient of total pressure along the vortex-core centerline is shown in Fig. 11b. $C_{p,\text{total}}$ is defined as $(p_{\text{total}} - p_{\text{total,ref}})/q_{\text{ref}}$. The experiment exhibits a steady monotonic decrease of total pressure along the vortex core at about a rate of 0.77 units per chord length of downstream distance. Note that the vertical-axis range of $C_{p,\text{total}}$ encompasses only 1.6 units, compared with the 4.0 units covered by that of the plot of $C_{p,\text{static}}$, which makes the decrease of $C_{p,\text{total}}$ appear more drastic than it really is. The decrease in $C_{p,\text{total}}$ is expected, as viscosity dissipates kinetic energy into heat. The SA-RC and ASM cases exhibit decreases in total pressure with downstream distance at rates of 0.06 and 0.10 units per chord, respectively; the rates are not nearly as steep as in the experiment. The SA-RC case exhibits a slight increase in $C_{p,\text{total}}$ near the downstream boundary, which may be a spurious boundary effect. Both the SA and SST cases exhibit decreases in $C_{p,\text{total}}$ more like the experiment than the SA-RC or ASM cases between $-0.4c < x < 0.1c$ and $-0.4c < x < 0.3c$, respectively. After those regions, however, $C_{p,\text{total}}$ increases drastically toward an asymptotic value of about 0.8. The minima of $C_{p,\text{total}}$ in these cases do not correspond to the respective maxima of axial velocity (Fig. 11c) in the vortex core. The fact that $C_{p,\text{total}}$ increases along the core in these cases seems unphysical because viscosity dissipates energy as the flow moves downstream. Also, it is not understood why the best-performing SA-RC model exhibits such different behavior from that of the experiment or why the SA-RC case does not exhibit the large initial decrease in $C_{p,\text{total}}$ as in the SA case.

Axial Velocity. The axial velocity along the vortex-core centerline is shown in Fig. 11c. The experimental measurements of axial velocity show that as the vortex forms, an axial velocity excess develops. In other words, jetlike behavior exists in the vortex core. The velocity excess peaks at $x = 0$ with a value of around $1.77U_{\text{ref}}$, after which the velocity gradually decreases to about $1.70U_{\text{ref}}$ at $x = 0.6c$. The SA-RC case is the only computational case that exhibits core axial velocity in good agreement with the experiment. In this case, the peak velocity excess is $1.78U_{\text{ref}}$, slightly greater than in the experiment. However, the excess decays more gradually than in the experiment. All other cases exhibit a velocity excess peak at around $x = 0$, as in the experiment, but the excess quickly becomes a deficit. In the SST and SA cases, the velocity excesses more quickly change to deficits than in the ASM case. The axial velocity in the SST and SA cases continues to decay to $U = 0.8U_{\text{ref}}$, followed by a gradual increase of velocity that asymptotically approaches U slightly less than U_{ref}. The ASM case exhibits the greatest core axial velocity excess of $U = 1.96U_{\text{ref}}$ at $x = 0$. This excess then decays and becomes a deficit at $x = 1.5c$. Beyond $x = 1.5c$ the axial velocity continues to decay with no asymptotic behavior observed, such that the core axial velocity is $U = 0.5U_{\text{ref}}$ at $x = 3c$. The SA and SST models seem to predict vortices that are so diffuse that even their erroneous wakelike behavior diminishes as they diffuse and lose strength. The vortex of the ASM case behaves differently from those of all the other cases. The ASM case's vortex exhibits the largest jetlike behavior and then develops wakelike behavior that builds in intensity with downstream distance. One could conclude that the ASM model is diffusive like the SA and SST models, but diffusive at a slower rate. It is interesting to note that the ASM model's behavior as measured by both $C_{p,\text{static}}$ and U/U_{ref} follows the same trends as Kim and Rhee's [20] computed results, which were obtained using FLUENT's Reynolds stress model. Although the ASM is different from a full Reynolds stress model, its formulation is based on a full Reynolds stress model, and so it may be expected to perform similarly.

Core Radius. Core radius, which is defined as the distance from the core centerline to the location of peak tangential velocity, is indicative of how large a role turbulence plays in radial diffusion of mean momentum. Figure 11d shows a plot of circumferentially averaged core radius $r_{c,\text{avg}}$. The experimental data show that $r_{c,\text{avg}}$ at $x = -0.4c$ is $0.021c$, and it increases to a maximum of $0.028c$ at $x = 0.25c$. Downstream of this location, $r_{c,\text{avg}}$ remains fairly constant. This behavior is well predicted by the SA-RC model, in which the maximum $r_{c,\text{avg}}$ occurs at $x = 0.20c$, slightly upstream of that of the experiment. Here, the radius is $0.032c$, which is 14% larger than in the experiment. After $x = 0.20c$, the core radius decreases by $0.002c$ and then remains fairly constant. The ASM case predicts a core size consistent with, but slightly smaller than, that of the experiment along $x < 0.5c$. Beyond $x = 0.5c$, the core radius in the ASM case grows nearly linearly at a rate of $0.023c$ per chord of axial distance. The SST and SA cases predict cores that grow nearly linearly beyond $x = -0.4c$ at about twice the rate of the ASM case, but the SST case exhibits a slightly larger core growth rate than the SA case.

Core Location. All cases well predict core location in the x–y plane, as shown in Fig. 11e. In the x–z plane, shown in Fig. 11f, the SA case predicts the vortex to be too far inboard at $x = -0.1c$, whereas all other cases are in good agreement with the experiment. Interestingly, the SA-RC and ASM cases predict more oscillation of the vortex-core location than the SST or SA models. The SA-RC and ASM cases predict stronger secondary and tertiary vortices, and the oscillations may be caused by those vortices interacting and merging with the primary vortex.

Turbulence Results

In the previous discussion, it is clear that the mean flow results from the case using the SA-RC turbulence model are most in agreement with the experiment. The nonrotation corrected SA and SST models predict far more diffuse vortices that have core radii that steadily increase with downstream distance. The performance of the ASM model lies somewhere in between. Certain details from the ASM case, such as vortex formation or wing-surface shear stresses, are more similar to the SA-RC case, though. Turbulence quantities may provide an explanation for these differences in the computed mean flow.

When comparing the computed and experimental turbulence quantities, it is important to note that vortex meander has an effect on the levels of these quantities. To capture vortex meander with CFD, unsteady computations are necessary. Although steady computations have been performed in this study, comparison with the experiment is still made. Chow [6] commented that because his measurements were taken near the wing's trailing edge, the effects of meander are minimized.

Turbulent Kinetic Energy

Turbulent kinetic energy k is important because it quantifies the energy contained within the turbulent part of the flow. Of the turbulence models used in this study, only the SST and ASM models compute k. Figure 12 shows radial profiles of circumferentially averaged turbulent kinetic energy in the wingtip vortex at various streamwise locations. Chow's [6] experimental data (Fig. 12a) show that peak k initially lies at the edge of the vortex core at $x = 0.005c$. This peak grows then rapidly decays, leaving a new peak along the centerline near $x = 0.246c$; then the entire k profile decays with downstream distance. It is interesting that for $x \geq 0.246c$, the peak of k lies within the core of the wingtip vortex, in which there is solid-body rotation, which is often thought to suppress turbulence. Instead, it seems that turbulence is being predominantly suppressed near the vortex-core edge.

Compared with the other computations, the SST case, shown in Fig. 12b, exhibits the most diffuse vortex, based on the fact that its vortex core grows most quickly with downstream distance, as seen in Fig. 11d. This is reflected by the fact that the predicted peaks of k in the SST case are an order of magnitude larger than those measured in the experiment. The SST model predicts the peak of k to always be at the vortex centerline, which does not agree with the experiment. Also, the SST model predicts that peak k grows and then decays within the range $0.005c \leq x \leq 0.678c$.

In contrast, the ASM case, shown in Fig. 12c, exhibits peak magnitudes of k between one-quarter and one-half of those measured in the experiment. Unlike in the experiment, the peak of k in this case never lies on the vortex centerline: rather, it initially lies on the vortex-core edge at $x = 0.005c$ and moves inboard to $r = 0.7r_{c,\text{avg}}$ at

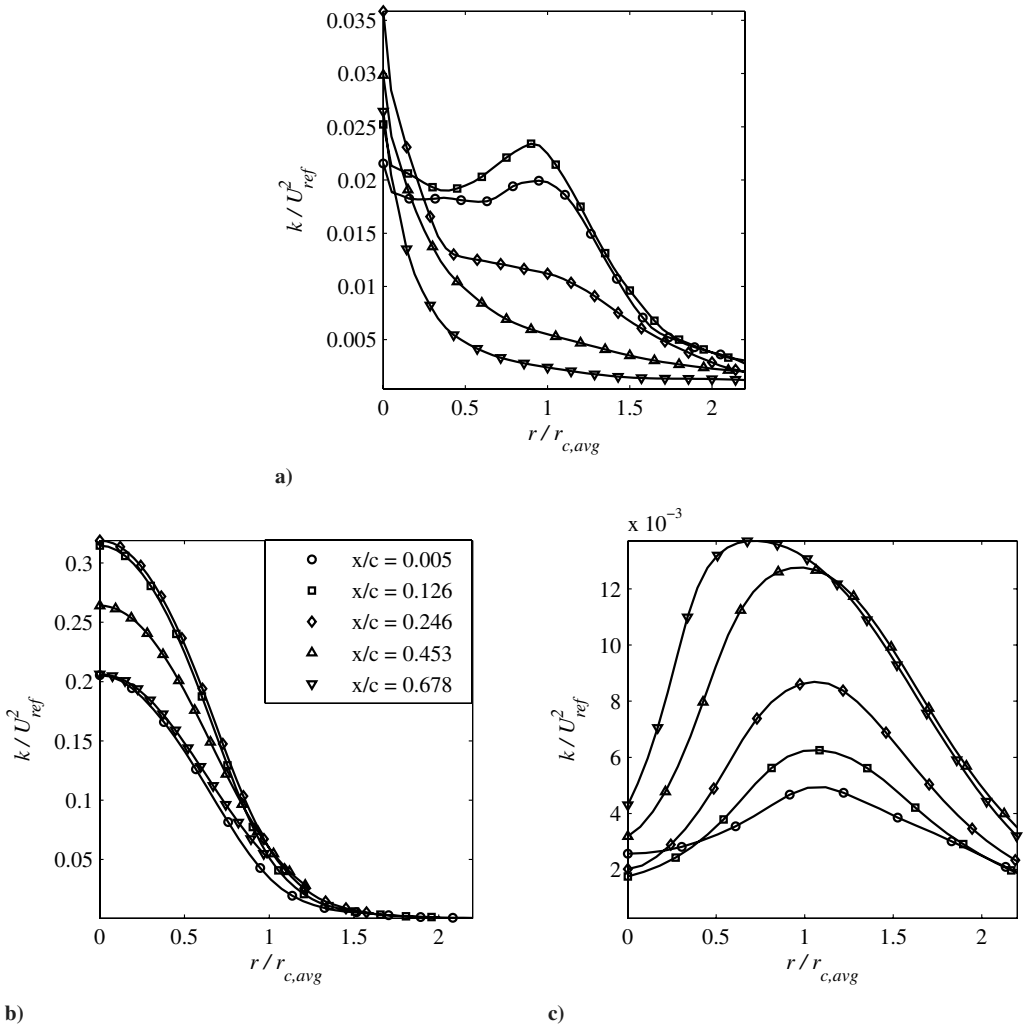

Fig. 12 Circumferentially averaged k normalized by U^2_{ref} radial profiles through the vortex at various downstream locations: a) experiment, b) SST, and c) ASM.

$x = 0.678c$. Also, this peak only grows within the range $0.005c \leq x \leq 0.678c$; no decay is shown as in the experiment.

The SST case exhibits peak k that grows then decays, whereas the ASM case exhibits peak k that grows but does not decay. This behavior reinforces the idea that the ASM model is diffusive like the SST and SA models, but diffusive at a slower rate.

Turbulent Viscosity

Turbulent viscosity is a quantity that all four turbulence models compute. Figure 13 shows circumferentially averaged radial profiles of ν_t at various axial locations. It is interesting to note the variation in the order of magnitude of the profiles for each different case. The SST and SA models, shown in Figs. 13a and 13c, respectively, both predict peak ν_t along the vortex centerline with values on the order of 10^4. Both the SA and SST models predict ν_t to grow and never decay with downstream distance.

The turbulent viscosity profiles of the SA-RC and ASM cases, shown in Figs. 13b and 13d, respectively, are different from those of the SA and SST cases. The SA-RC model predicts peak levels of ν_t on the order of 10^2, whereas the ASM case predicts them to be on the order of 10^3, 1–2 orders of magnitude less than that predicted by the SA or SST models. Both the SA-RC and ASM models predict the peaks of ν_t to lie at $r \geq r_{c,\text{avg}}$, rather than on the centerline. In the SA-RC case, centerline ν_t is equal to 50 times the molecular viscosity at $x = 0.005c$, and it decays to nearly zero by $x = 0.678c$. The centerline ν_t of the ASM case is always nearly zero. The peak ν_t predicted by the SA-RC model decays and diffuses outward with downstream distance, whereas that of the ASM case grows and remains fixed at $r = 1.3r_{c,\text{avg}}$. It is interesting that the ASM naturally reduces ν_t within the vortex's region of solid-body rotation, similar to the behavior of the SA-RC model, due to its rotation correction term.

Although not shown here, contour slices of ν_t through the vortex axis at various locations downstream of the wing show an interesting difference in behavior between the ASM and SA-RC models. In the contours from the ASM case, suppression of ν_t seems to occur only very near the centerline. Contours from the SA-RC case, though, indicate that suppression of ν_t begins where streamlines from the wake begin to curve as they are wrapped around the vortex. This suppression of ν_t continues inward to the vortex centerline.

Reynolds Stresses

Because of the Cartesian reference frame, contours of Reynolds shear stress components plotted in the y–z planes through the vortex exhibit distinct positive and negative lobes. The $\langle u'v' \rangle$ and $\langle u'w' \rangle$ components each have a positive and a negative lobe. The lobes are oriented opposite to each other and those of the $\langle u'v' \rangle$ component are rotated 90 deg from those of the $\langle u'w' \rangle$ component. The $\langle v'w' \rangle$ component has four lobes of alternating sign oriented in a four-leaf-clover pattern. The corresponding components of the mean strain-rate tensor exhibit similar qualities. Because similar comparisons between experiment and computation can be made for all three Reynolds shear stress components, only the $\langle v'w' \rangle$ component is examined here. Contour plots of that component from the experiment and computations at $x = 0.452c$ are shown in Fig. 14. This location is chosen because the vortex is well formed and nearly axisymmetric here.

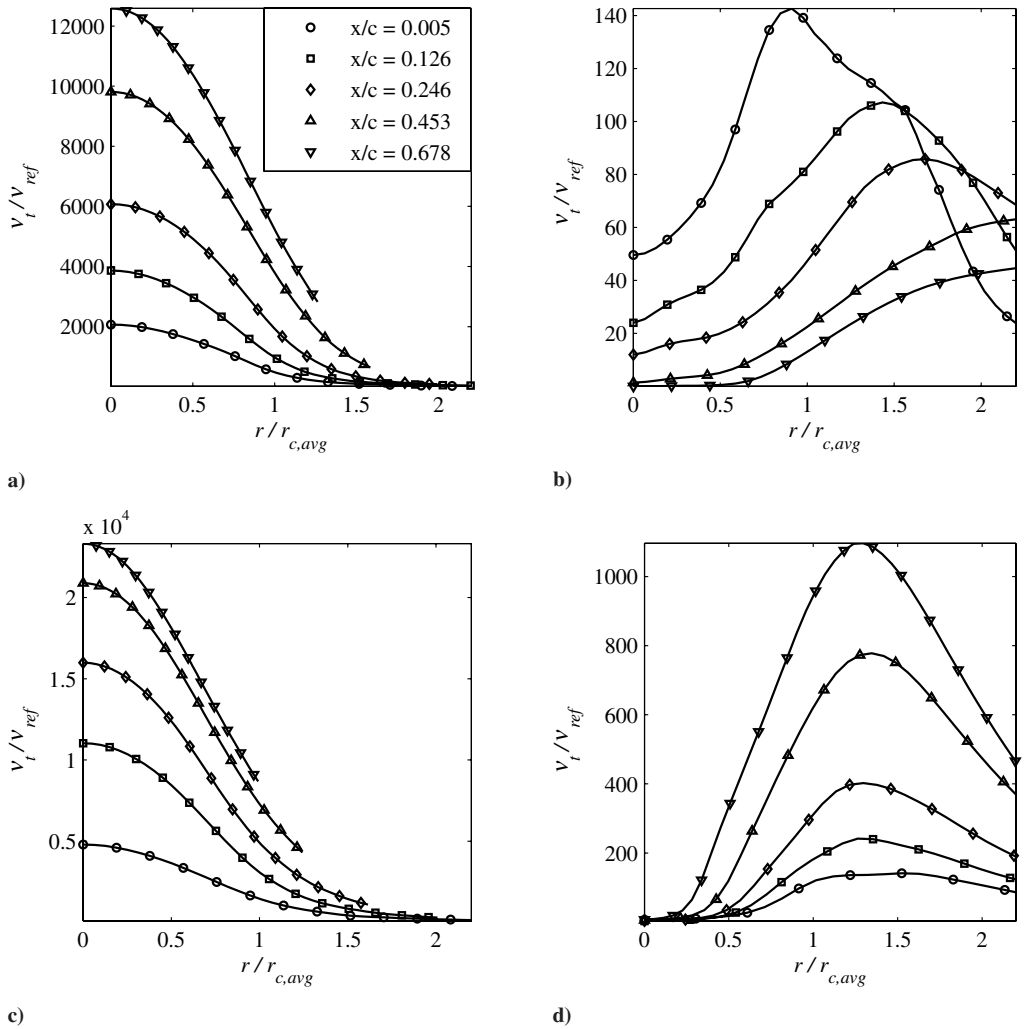

Fig. 13 Circumferentially averaged ν_t normalized by ν_{ref} radial profiles through vortex at various downstream locations: a) SA, b) SA-RC, c) SST, and d) ASM.

One of the most prominent features of the contour plot of $\langle v'w' \rangle$ measured in Chow's [6] experiment, shown in Fig. 14b, is that the contour lobes are not aligned with the lobes of the corresponding component of the strain-rate tensor, shown in Fig. 14a. Rather, they are rotated clockwise by roughly 45 deg when viewed from downstream looking upstream. Following a streamline, one can see that the Reynolds stress lags behind the strain rate. This happens because the Reynolds stresses require time to react to the changing mean flow. The contours of $\langle v'w' \rangle$ predicted with the SA, SA-RC, and SST models, shown in Figs. 14c–14e, all have their lobes oriented the same as the corresponding strain rate. This is because these models are linear turbulent viscosity models, meaning that they calculate Reynolds stresses from the Boussinesq approximation of Eq. (1). The Boussinesq approximation dictates that the Reynolds stress tensor is proportional to the mean strain-rate tensor, and so no lag can occur. In contrast, the ASM calculates Reynolds stresses from a nonlinear relation between turbulent and mean parts of the flow. This nonlinearity allows for lag to occur, which is apparent in Fig. 14f. This contour plot shows that the lobes of $\langle v'w' \rangle$ are rotated clockwise, but not as much as observed in the experiment. However, the contour plots of the other Reynolds shear stress components computed with the ASM are tilted in the opposite direction from those observed in the experiment.

Furthermore, the computed magnitudes of $\langle v'w' \rangle$ are not the same as those of the experiment. The limits of the contour levels for all computational cases had to be set differently from that of the experiment so that all contour levels are shown. As expected, because the SA and SST cases predict a more diffuse vortex than observed in the experiment, they exhibit peak $\langle v'w' \rangle$ contours nearly 4 times as large as that of the experiment at $x = 0.452c$. The better-performing ASM and SA-RC models exhibit peak contours of $\langle v'w' \rangle$ that are 1 and 2 orders of magnitude lower than in the experiment, respectively, at this location. Therefore, although the SA-RC model predicts many features of the mean flow correctly, it greatly underpredicts the level of turbulent shear stress.

Conclusions

Computations of a wingtip-vortex flow in the near field are performed using NPARC's WIND flow solver to assess the performance of various popular aerodynamics turbulence models. The models explored are the one-equation Spalart–Allmaras model in both standard form (SA) [29,30] and with the Spalart–Shur correction for system rotation and streamline curvature (SA-RC) [13–15], the Menter two-equation shear stress transport (SST) k-ω model [31,32], and the Rumsey–Gatski k-ϵ algebraic Reynolds stress model (ASM) [33–35]. The effects of grid resolution and numerical scheme are also addressed. The computed flow is compared with the mean and turbulent measurements of a wingtip vortex gathered by Chow et al. [5–7]. The vortex-generating wing is a simple straight half-wing with its root mounted to one of the vertical walls of a wind tunnel. The chord-based Reynolds number is 4.6×10^6.

It was found that the SA-RC model performs best when predicting the vortex mean flow. It is able to predict vortex centerline static pressure to within 9.4% of that of the experiment. It also predicts centerline axial velocity only 0.6% different from that measured in

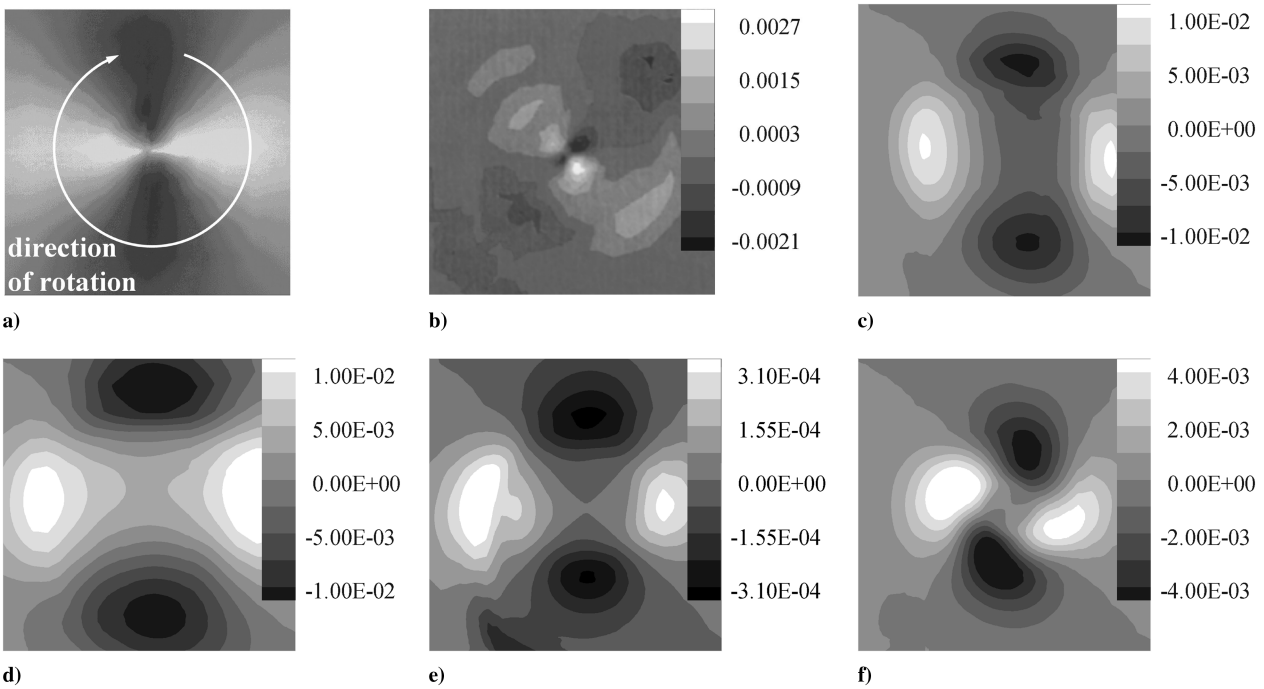

Fig. 14 Contour plots of strain-rate and Reynolds stress components: a) the $-S_{23}$ strain-rate component from the experiment. Contour plots of the $\langle v'w' \rangle$ Reynolds shear stress component normalized by U_{ref}^2 at $x = 0.452c$ from b) experiment, c) SA, d) SST, e) SA-RC, and f) ASM. Contours are viewed from downstream looking upstream (images from the experiment are reproduced from [6] with the author's permission).

the experiment. The SA-RC case is the only one to predict the vortex of a nearly unchanging (as opposed to rapidly growing) core radius, which more closely resembles the behavior observed in Chow's [6] experiment. The SA and SST models perform the most poorly in this highly rotational flow. They predict far-too-diffuse vortices. The ASM performs better than the SA and SST models but not as well as the SA-RC model. It predicts too diffuse a vortex, but the vortex diffuses at a slower rate with downstream distance than with the SA and SST models. However, the ASM performs comparable with the SA-RC model at predicting other details of the mean flow, such as the vortex-formation process and wing-surface stresses.

In this study, it becomes apparent that each of the turbulence models considered has deficiencies. Although the SA-RC model computes the mean flow well, it predicts Reynolds shear stresses with peak values an order of magnitude lower than those of the experiment. In contrast, the SA and SST models predict Reynolds shear stresses that are an order of magnitude greater than in the experiment, and thus the mean flow is not as well predicted. The SA-RC model and the ASM both predict a suppression of turbulent viscosity within the vortex core, but each model differently predicts the radial extent of this suppression. To accomplish this suppression, the SA-RC model uses an empirical rotation correction, and the ASM relies upon its nonlinear relation between the Reynolds stress and mean strain-rate tensors. The SST model and the ASM are the only models we examined that compute turbulent kinetic energy, and neither model predicts the important change of the radial location of the peak turbulent kinetic energy with downstream distance; in the experiment, a peak at the core edge decays, leaving a new peak at the core centerline. Although not the best-performing model, the ASM is the only model able to predict the lag of some of the Reynolds stress components behind the corresponding strain-rate components, which is true of the experiment; however, the ASM also predicts a lead in other Reynolds shear stress components.

It was also learned that creating a computational grid for this type of flow is tedious and time-consuming. A grid of H-topology with 5.3×10^6 points is used and is well suited to this type of geometry. This topology is recommended for future work, especially in cases in which overset grids are not an option. However, an overset-grid system may be more flexible. It could include a C-topology grid around the wing and wingtip, an independent H-topology grid in the vortex core with as many points as required, and coarser H-topology grids elsewhere. There are many important regions of the flow that exhibit large gradients for which fine grid spacing is required, such as the wing boundary layer, the wake, and the vortex core. Difficulties arise because these regions feed into one another. The vortex core seems especially sensitive to grid density and spatial order of accuracy of the numerical scheme. In this study, we use 21 grid points across the spanwise and vertical extents of the vortex-core cross section, and we manually adapt the grid to follow the core's location downstream. This seems adequate when a spatially-fifth-order numerical scheme is used. Although not the same as performing grid refinement, the use of one of WIND's spatially-higher-order numerical schemes improves the solution accuracy without as much computational cost as adding grid points. This is an attractive option if the user's computational resources are limited.

The main areas that need improvement to better compute wingtip-vortex flows are turbulence modeling and the grid generation and refinement process. There is a need for a turbulence model, not much more complex than current two-equation models, that better captures turbulence physics in rotating flows while still performing well in nonrotating regions. The grid generation and refinement process needs to be improved because grid quality has a large effect on solution accuracy. Generating a complex grid is tedious, and refinements to that grid often require hours of manipulation by the user, even when using sophisticated grid generation software. Although not used in this study, adaptive grid refinement is a powerful tool that could streamline the grid generation and refinement process.

Acknowledgments

The first author has been supported by a Purdue University Lynn Fellowship from the Computational Science and Engineering Program and a National Science Foundation Graduate Research Fellowship. Jim Chow and Peter Bradshaw provided the experimental data and useful advice. Xavier Tricoche of Purdue University's Computer Science Department has been insightful and helpful in effectively visualizing the secondary and tertiary vortices and surface streamlines observed in this flow. He is responsible for creating the line-integral-convolution visualizations used in Fig. 8 and for providing useful advice in creating the secondary and tertiary

streamline visualization of Fig. 10b. Furthermore, Chris Nelson of the Innovative Technology Applications Company, LLC, has answered any WIND-related questions that arose. The computations were performed on a LINUX cluster belonging to Purdue University's School of Aeronautics and Astronautics. The cluster was acquired using a Defense University Research Instrumentation Program (DURIP) grant sponsored by the U.S. Army Research Office.

References

[1] Rossow, V. J., "Lift-Generated Vortex Wakes of Subsonic Transport Aircraft," *Progress in Aerospace Sciences*, Vol. 35, No. 6, Aug. 1999, pp. 507–660. doi:10.1016/S0376-0421(99)00006-8

[2] "Airbus A380 Wake Vortex—Revised Guidance Material," *The Fifth Meeting of the FANS Implementation Team (FIT-SEA/5)*, International Civil Aviation Organization, Bankok, Thailand, Jan. 2006, http://www.icao.int/icao/en/ro/apac/2007/FIT_SEA5/ip05.pdf [retrieved 4 Feb. 2008].

[3] Gerz, T., Holzäpfel, F., and Darracq, D., "Commercial Aircraft Wake Vortices," *Progress in Aerospace Sciences*, Vol. 38, No. 3, Apr. 2002, pp. 181–208. doi:10.1016/S0376-0421(02)00004-0

[4] Spalart, P. R., "Airplane Trailing Vortices," *Annual Review of Fluid Mechanics*, Vol. 30, Jan. 1998, pp. 107–138, doi:10.1146/annurev.fluid.30.1.107.

[5] Chow, J. S., Zilliac, G. G., and Bradshaw, P., "Measurements in the Near-Field of a Turbulent Wingtip Vortex," AIAA Paper 1993-0551, Jan. 1993.

[6] Chow, J. S., "Turbulence Measurements in the Near-Field of a Wingtip Vortex," Ph.D. Thesis, Dept. of Mechanical Engineering, Stanford Univ. , Stanford, CA, Aug. 1994.

[7] Chow, J. S., Zilliac, G. G., and Bradshaw, P., "Mean and Turbulence Measurements in the Near Field of a Wingtip Vortex," *AIAA Journal*, Vol. 35, No. 10, Oct. 1997, pp. 1561–1567. doi:10.2514/2.1

[8] Zilliac, G. G., Chow, J. S., Dacles-Mariani, J., and Bradshaw, P., "Turbulent Structure of a Wingtip Vortex in the Near Field," AIAA Paper 1993-3011, July 1993.

[9] Dacles-Mariani, J., Rogers, S., Kwak, D., and Zilliac, G. G., "A Computational Study of Wingtip Vortex Flowfield," AIAA Paper 1993-3010, July 1993.

[10] Dacles-Mariani, J., Zilliac, G. G., Chow, J. S., and Bradshaw, P., "Numerical/Experimental Study of a Wingtip Vortex in the Near Field," *AIAA Journal*, Vol. 33, No. 9, Sept. 1995, pp. 1561–1568. doi:10.2514/3.12826

[11] Dacles-Mariani, J., Kwak, D., and Zilliac, G. G., "Accuracy Assessment of a Wingtip Vortex Flowfield in the Near-Field Region," AIAA Paper 1996-0208, Jan. 1996.

[12] Dacles-Mariani, J., Kwak, D., and Zilliac, G. G., "On Numerical Errors and Turbulence Modeling in Tip Vortex Flow Prediction," *International Journal for Numerical Methods in Fluids*, Vol. 30, May 1999, pp. 65–82. doi:10.1002/(SICI)1097-0363(19990515)30:1<65::AID-FLD839>3.0.CO;2-Y

[13] Shur, M., Strelets, M., Travin, A., and Spalart, P. R., "Two Numerical Studies of Trailing Vortices," AIAA Paper 1998-0595, Jan. 1998.

[14] Spalart, P. R., and Shur, M., "On the Sensitization of Turbulence Models to Rotation and Curvature," *Aerospace Science and Technology*, Vol. 1, No. 5, 1997, pp. 297–302. doi:10.1016/S1270-9638(97)90051-1

[15] Shur, M., Strelets, M., Travin, A., and Spalart, P. R., "Turbulence Modeling in Rotating and Curved Channels: Assessment of the Spalart–Shur Correction Term," AIAA Paper 1998-0325, Jan. 1998.

[16] Duraisamy, K., and Baeder, J. D., "Numerical Simulation of the Effects of Spanwise Blowing on Wing-Tip Vortex Formation and Evolution," AIAA Paper 2005-4726, June 2005.

[17] Duraisamy, K., and Baeder, J. D., "Numerical Simulation of the Effects of Spanwise Blowing on Tip Vortex Formation," *Journal of Aircraft*, Vol. 43, No. 4, July–Aug. 2006, pp. 996–1006. doi:10.2514/1.19746

[18] Duraisamy, K., and Iaccarino, G., "Curvature Correction and Application of the v^2-f Turbulence Model to Tip Vortex Flows," Center for Turbulence Research, Stanford Univ., Stanford, CA, 2005, pp. 157–168, http://www.stanford.edu/group/ctr/ResBriefs/temp05/duraisamy.pdf [retrieved 23 Feb. 2006].

[19] Durbin, P. A., "Near-Wall Turbulence Closure Modeling Without 'Damping Functions,'" *Theoretical and Computational Fluid Dynamics*, Vol. 3, No. 1, Sept. 1991, pp. 1–13.

[20] Kim, S., and Rhee, S., "Prediction of Tip-Vortex Flow Past a Finite Wing," AIAA Paper 2005-0058, Jan. 2005.

[21] Uzun, A., Hussaini, M. Y., and Streett, C. L., "Large-Eddy Simulation of a Wing Tip Vortex on Overset Grids," *AIAA Journal*, Vol. 44, No. 6, June 2006, pp. 1229–1242. doi:10.2514/1.17999

[22] Bush, R. H., Power, G. D., and Towne, C. E., "WIND–The Production Flow Solver of the NPARC Alliance," AIAA Paper 1998-0935, Jan. 1998.

[23] *WIND User's Guide*, Ver. 5.0, 2007, http://www.grc.nasa.gov/WWW/winddocs/wind5.0/user/user.pdf [retrieved 11 July 2007].

[24] *Wind-US User's Guide*, Ver. 1.0, 2007, http://www.grc.nasa.gov/WWW/winddocs/windus1.0/user/user.pdf [retrieved 11 July 2007].

[25] Bush, R. H., "A Three Dimensional Zonal Navier–Stokes Code for Subsonic Through Hypersonic Propulsion Flowfields," AIAA Paper 1988-2830, July 1988.

[26] Roe, P. L., "Approximate Riemann Solvers, Parameter Vectors, and Difference Schemes," *Journal of Computational Physics*, Vol. 43, No. 2, Oct. 1981, pp. 357–372. doi:10.1016/0021-9991(81)90128-5

[27] Churchfield, M. J., and Blaisdell, G. A., "Near Field Wingtip Vortex Computation Using the WIND Code," AIAA Paper 2006-0633, Jan. 2006.

[28] Churchfield, M. J., "Numerical Computations of a Wingtip Vortex in the Near Field," Master's thesis, School of Aeronautics and Astronautics, Purdue University, West Lafayette, IN 47907, May 2006.

[29] Spalart, P. R., and Allmaras, S. R., "A One-Equation Turbulence Model for Aerodynamic Flows," AIAA Paper 1992-0439, Jan. 1992.

[30] Spalart, P. R., and Allmaras, S. R., "A One-Equation Turbulence Model for Aerodynamic Flows," *La Recherche Aérospatiale*, Vol. 1, No. 1, 1994, pp. 5–12.

[31] Menter, F. R., "Zonal Two Equation k-ω Turbulence Models for Aerodynamic Flows," AIAA Paper 1993-2906, July 1993.

[32] Menter, F. R., "Two-Equation Eddy-Viscosity Turbulence Models for Engineering Applications," *AIAA Journal*, Vol. 32, No. 8, Aug. 1994, pp. 1598–1605. doi:10.2514/3.12149

[33] Rumsey, C. L., Gatski, T. B., and Morrison, J. H., "Turbulence Model Predictions of Strongly Curved Flow in a U-Duct," *AIAA Journal*, Vol. 38, No. 8, Aug. 2000, pp. 1394–1402. doi:10.2514/2.1115

[34] Rumsey, C. L., and Gatski, T. B., "Recent Turbulence Model Advances Applied to Multielement Airfoil Computations," *Journal of Aircraft*, Vol. 38, No. 5, Sept.–Oct. 2001, pp. 904–910. doi:10.2514/2.2850

[35] Yoder, D., "Initial Evaluation of an Algebraic Reynolds Stress Model for Compressible Turbulent Shear Flows," AIAA Paper 2003-0548, Jan. 2003.

[36] Haimes, R., and Kenwright, D., "On the Velocity Gradient Tensor and Fluid Feature Extraction," AIAA Paper 1999-3288, June–July 1999.

[37] Mathews, J. H., *Numerical Methods for Computer Science, Engineering, and Mathematics*, Prentice–Hall, London, 1987, pp. 270–274.

[38] Cabral, B., and Leedom, L., "Imaging Vector Fields Using Line Integral Convolution," *Proceedings of the 20th Annual Conference on Computer Graphics and Interactive Techniques (SIGGRAPH '93)*, ACM Press, New York, 1993, pp. 263–270.

[39] Tricoche, X., Garth, C., and Sheuermann, G., "Fast and Robust Extraction of Separation Line Features," *Scientific Visualization: The Visual Extraction of Knowledge from Data*, edited by G.-P. Bonneau, T. Ertl, and G. M. Nielson, Springer–Verlag, New York, 2006, pp. 249–263.

[40] Tricoche, X., Garth, C., Kindlmann, G., Deines, E., Scheuermann, G., Ruetten, M., and Hansen, C., "Visualization of Intricate Flow Structures for Vortex Breakdown Analysis," *IEEE Visualization 2004*, Inst. of Electrical and Electronics Engineers, Piscataway, NJ, Oct. 2004, pp. 187–194, doi:10.1109/VISUAL.2004.113.